
PHOTOGRAMMETRIC CALIBRATION OF RANGE IMAGING SENSORS USING INTENSITY AND RANGE INFORMATION SIMULTANEOUSLY

*Patrick Westfeld, Christian Mulsow and Marc Schulze
Institute of Photogrammetry and Remote Sensing
Technische Universität Dresden
Email: patrick.westfeld@tu-dresden.de*

Abstract: The article presents and discusses the results of an integrated photogrammetric 3-D camera calibration approach. These include the interior camera orientation parameters with their standard deviations and the estimation of accuracy specifications for each introduced observation group (i.e. image coordinates measured in 3-D camera intensity and range images as well as the slant ranges) from variance component estimation. Furthermore, the expansion to additional distance calibration terms is discussed.

1. Introduction

Range imaging (RIM) cameras based on photonic mixer devices (PMD) provide simultaneous gray value and distance measurements of the scene in each pixel of the sensor. As a result, a spatiotemporal resolved representation of the object space is given in the form of intensity images and range maps. In the field of RIM sensor technology, 3-D cameras are currently available with a sensor size of up to 40,000 pixels and a frame rate of up to 50 Hz. Advantages of this new 3-D mapping technology are the simultaneous generation of 3-D surface data on a discrete raster with a high repeat rate as well as the marginal dimension and acquisition costs. Drawbacks are the limited range, the small spatial resolution and the sensitivity against background illumination.

Precise 3-D object registration takes an important weight in many scientific and applied areas. In recent decades, Photogrammetry becomes an accepted and powerful instrument for tasks in 3-D data acquisition, measurement and analysis. Using conventional analog or digital close-range cameras, the reference between image sensor and object space is given by the interior (IOR) and exterior (EOR) orientation parameters as well as the 2-D pixel and 3-D object coordinates. In this context, focal length, principal point and lens distortions compensate for deviations from an ideal pinhole camera model. Ideal central perspective geometry is assumed for the on-chip calculation of 3-D camera Cartesian coordinates, too (e.g. [4]). According to the required accuracy specifications as well as environmental conditions, deviations of this ideal model have to be handled by suitable calibration techniques.

Up to now, several approaches for photogrammetric 3-D camera calibration have been introduced. Kahlmann [5], Lindner&Kolb [9] or Robbins et al. [11] observe planar target plates in intensity images to perform a photogrammetric camera self-calibration. With respect to RIM data it appears desirable to utilize the additional range information for integrated calibration

techniques. Karel [6] and Lichti [8] use intensity image sequences for the determination of targets' pixel coordinates and range maps to derive a distance observation for each target. All observations are introduced into a bundle adjustment, which results in calibration parameters for the IOR and EOR as well as a distance correction term. Schiller et al. [11] also propose a joint approach for photogrammetric and depth calibration using a multi-camera setup (one 3-D camera and multiple 2-D CCD cameras).

Westfeld [14] shows a simultaneous calibration approach for IOR parameter estimation utilizing all available 3-D camera information simultaneously (i.e. target's pixel coordinates from intensity and range images as well as the slant range between projection center and targets in object space). The approach shown here is based on this preliminary work and presents efforts on control point determination, image point measurement in both intensity and range image as well as the functional and stochastic model of an integrated spatial resection.

2. Experimental Setup

The data were captured by a *SwissRanger SR-3000* (Mesa Imaging AG, Zurich, CH). The integration time was set to 80.8ms, the modulation frequency to 20 MHz.

The reference field was designed taking into account the low spatial resolution of typical range cameras. Avoiding a large dimensioned reference field, a small calibration plate was designed, signalized with four white spheres only (Fig. 1).



Fig. 1: Intensity and gray scale coded range image of a 3-D calibration plate.

A 3-D reference field can be simulated by moving the calibration plate through the measurement volume: 3 depth layers; 2 height layers per depth layer; 3 positions of the plate per layer. This sequential image recording approach allows an adequately large number of spatially distributed targets to be captured from one 3-D camera position. The instantaneous field of view (IFOW) was $47.5 \times 39.6^\circ$. The sphere diameters are 100 mm, which correspond to 8 pixel in image space at a maximum distance of 2.5 m. Spheres close to the camera are at a minimum distance of 1.4 m with a diameter of 14 pixel. Due to the relationship between target size and achievable point accuracy [9], the theoretic accuracy potential of least-squares template matching in intensity images can be expected with 0.01-0.02 pixel (Sec. 4.1). Further important for the least-squares sphere fit in range images (Sec. 4.2) is the maximum number of pixel, which represent each sphere. Assuming the derived diameters, the area of an imaged sphere becomes at least 50 pixel.

3. Control Point Determination

In addition to the moving calibration target, a static reference field with small coded and non-coded targets is necessary to transform the central points of the spheres into a global coordinate system. The 3-D coordinates of all object points (static reference field targets and moving calibration plate targets) are determined successively by bundle adjustment and 3-D Hel-

mert-transformation based on multiple high resolution images taken by a conventional digital SLR camera *Nikon D100* with a 14 mm lens. The commercial software package *AICON 3D Studio* has been utilized for computation. As (a simplifying) alternative to this successive approach, a joint adjustment of all images should be considered.

First, the 3-D coordinates of the coded and non-coded targets have to be determined by usual bundle adjustment. This static reference field will be used as reference for the following Helmer-transformations. The mean point accuracies in image space are in the range of $1/40$ pixel, in object space in the range of 0.055 mm (lateral) resp. 0.082 mm (depth direction). The overall accuracy becomes $1/100$ pixel.

Second, the calibration plate is placed at 15 positions (Sec. 2). At each, one 3-D camera image is taken for the integrated spatial resection (Sec. 5), and multi spatially distributed SLR images are taken for one further bundle adjustment per calibration plate's position. At this, a mean accuracy of $1/30$ pixel for the image points and 0.036 mm (lateral) resp. 0.033 mm (depth direction) for the object points could be achieved.

Third, all epochs, including the several 3-D coordinates of the spheres, are transformed onto the reference frame. The residual discrepancies do not show any systematic effects and are in the range of 0.160 mm.

4. Image Point Measurement

Performing a spatial resection on the 3-D camera requires the image coordinates of the spheres. Besides usual point measurements in intensity images, the slant ranges as observations obtained directly are not only to be used for the adjustment. Rather image point coordinates achieved from range images should be integrated into the spatial resection. Thus it is possible to exploit the whole RIM information.

4.1. Intensity Image

The coordinates in gray value images $(x,y)^{gv}$ are measured straightforwardly by 2-D least-squares template matching (2-D LSM) with sub-pixel accuracy. The approximate values originate from an algorithm for automatic image point detection based on various image analysis functions like edge detection, thresholding and connectivity analysis [1]. 2-D LSM has been parameterized with two shifts in row and column and one scale only (view-independent sphere projection as circle). Furthermore, a 1-D student test has been implemented for testing parameter's level of significance ($p=0.95$). The mean standard deviation (SD) of the image points results in $1/40$ pixel (Fig. 2).

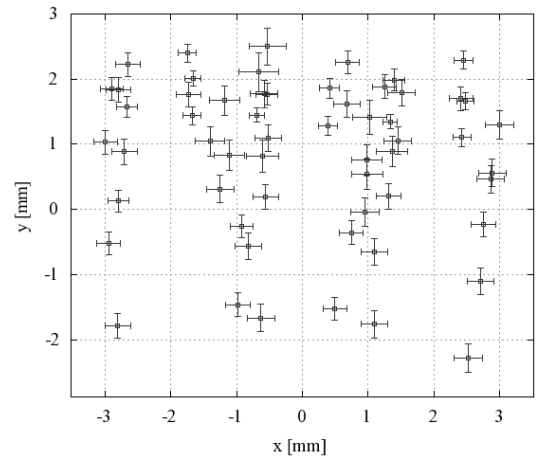


Fig. 2: SD of the intensity image points. $\bar{\sigma}_{x,y}^{gv} = 1/40$ pixel. Exaggeration: 200.

4.2. Range Image

The coordinates in the range value images $(x,y)^{rv}$ are measured by an image analysis scheme based on dynamic thresholding, RANSAC and sphere fit. Input values are discrete sensor po-

sitions, intensity values as well as range values scaled with reference to sensor's size. As a result, the range image coordinates of all centers of the spheres are available with sub-pixel accuracy. Additionally, the distance between each sphere and the corresponding sub-pixel in the range image is derived from the least-squares sphere fit, too.

First, approximate values obtained from Sec. 4.1 are used for a rough localization of the spheres. Two patches per sphere are cut out around the location of interest in both channels. All pixels within these patches are considered as possible candidates for the final sphere fit. Starting in the center of the range patch, a simple profile analysis in $\pm x$ and $\pm y$ is performed for further patch containment (Fig. 3). Consequently, the edges of the spheres and therewith first approximations of the diameters are obtained.

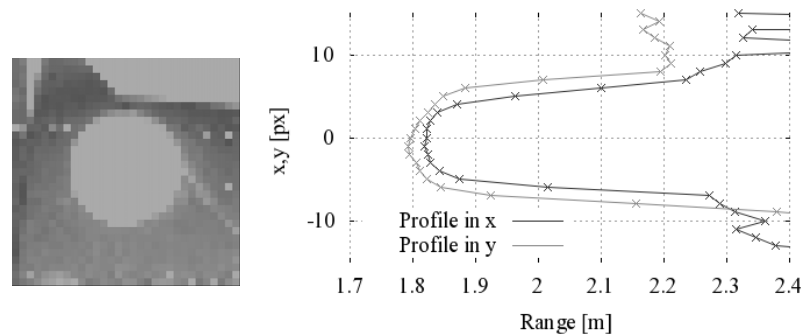


Fig. 3: Sphere-background-change detection: Range patch of interest (left) and corresponding range profiles (right).

Second, automatically determined intensity and range thresholds are applied. A black mat behind the white spheres absorbs the emitted 3-D camera infrared light nearly completely. Thus it is possible to derive a dynamic intensity threshold relatively easy by histogram analysis (Fig. 4). The range threshold is derived from profile analysis mentioned in the first step of processing.

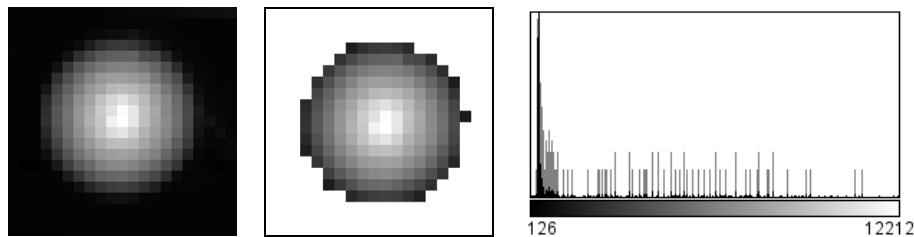


Fig. 4: Intensity threshold definition by histogram analysis: Intensity patch of interest (left) with applied intensity threshold (middle) and corresponding histogram (right).

Third, RANSAC (Random Sample Consensus) calculates the final initial set of observations and provides very good approximate values for the following least-squares sphere fit. RANSAC is an algorithm for robust parameter estimation [2] and is quite suited for RIM data containing a significant percentage of gross errors (due to the well known accuracy characteristic of 3-D cameras). The error tolerance for establishing the model compatibility and the lower bound on the size of an acceptable consensus set have been determined empirically. The maximum number of attempts to find a consensus set can be calculated.

Finally, all valid observations are introduced into a least-squares sphere fit, which is fully parameterized with three coordinates for the center and one radius. Solving the following system of observation equations for a general sphere

$$(x_{ik}^{rv} - x_k^{rv})^2 + (y_{ik}^{rv} - y_k^{rv})^2 + (rg_{ik}^{rv} - rg_k^{rv})^2 - r_k = 0 \quad (1)$$

with i : 1...Number of observations
 k : 1...Number of spheres
 $(x,y,rg)_{ik}^{rv}$: Image coordinates and corresponding range value observations

yield the unknown image coordinates $(x,y)_k^{rv}$ and the corresponding range value of the center rg_k^{rv} of each sphere k as well as the radius r_k . The resulting accuracy specifications for the unknown parameters are plotted in the following Fig. 5a-5c.

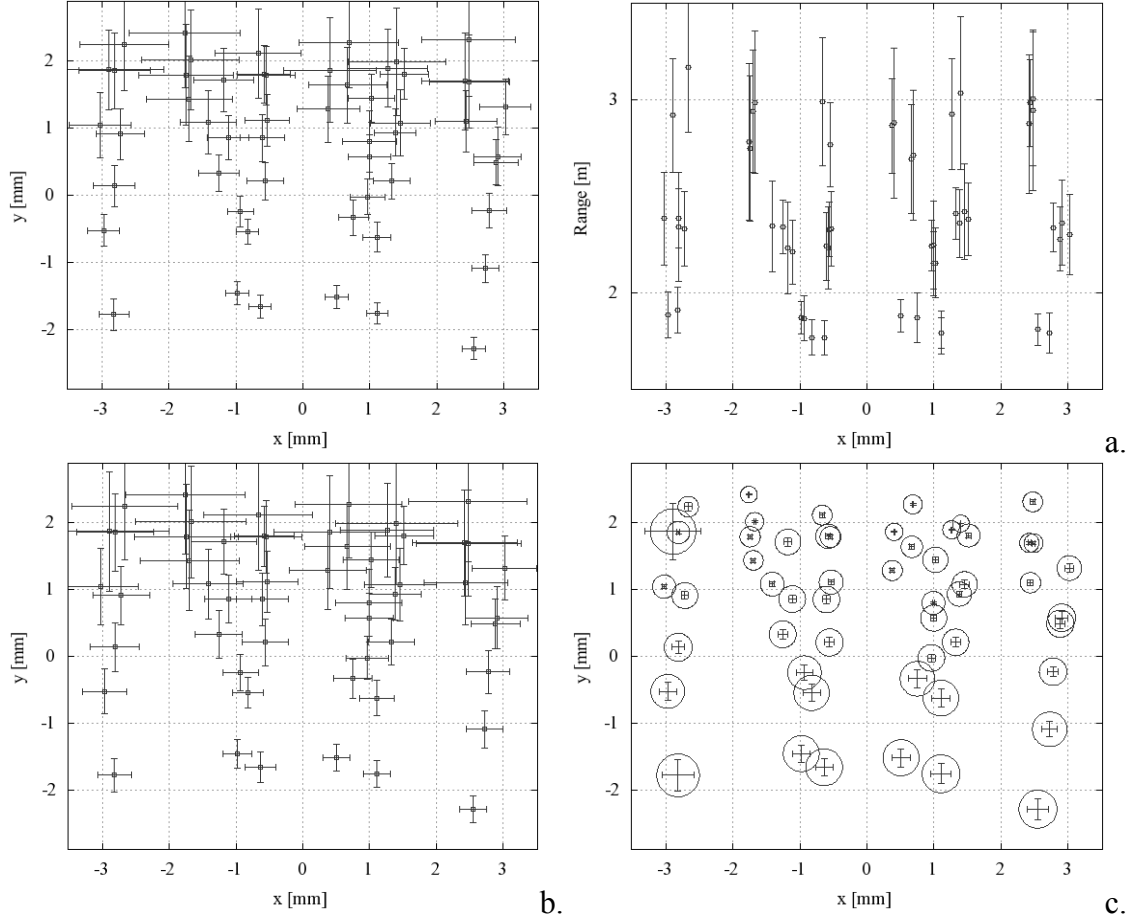


Fig. 5: Sphere fit accuracy specifications.

- a. SD of the centers of the spheres. $\bar{\sigma}_{x,y}^{rv} = 1/10$ pixel (left). $\bar{\sigma}_{rg}^{rv} = 1.54$ mm (right). Exaggeration: 200.
- b. SD of the radii. $\bar{\sigma}_r^{rv} = 1.00$ mm. Exaggeration: 0.5.
- c. 2-D plot of the estimated spheres with error bars representing nominal/actual variations of the radii. Center of the spheres within image space; radii and error bars are scaled with reference to sensor's size. Exaggeration: 2.

The centers of the targets can be obtained with an image point accuracy of $1/10$ pixel; thus 4 times worse in mean than the image point measurements in the intensity images. Further it is obvious that the precision of the distance measurement decreases with target's distance (Fig. 5a). Reasons for this are fewer observations for the sphere fits as well as the dependency of the distance measurement on the distance itself (cf. e.g. [5]). In the front layer of the moving reference field, an accuracy of $1/25$ pixel can be achieved; in the back layers, an accuracy of $1/5$ pixel only. The same conclusion can be made for the corresponding range values of the centers, which range between 0.62 mm and 2.72 mm. However, the mean becomes 1.54 mm and

reflects the relative precision of the distance measurements (cf. e.g. [3][13]). The accuracy of the estimated radii becomes 1.00 mm (Fig. 5b). Here, too, a distance dependency appears.

The mean radii in object space can be stated with 60.6 mm. This results in ca. 10 mm nominal/actual variations (Fig. 5c), which is quite consistent with the SD in centimeter level for a single distance measurement [5]. It is simply conspicuous that the variations increase from the back (4.8 mm) via the middle (8.4 mm) to the front target layer (17.8 mm). An experimental analysis follows.

4.3. Variations of Intensity and Range Image Measurements

Previous to a fully consideration of the two types of observations (within the stochastic model of the integrated adjustment introduced in Sec. 5.2), the variations between the image point measurements in both channels are of interest.

The plot in Fig. 6a shows small remaining systematic errors of the range image point measurement against the 2-D LSM results. Variations in x increase from the center to the boundaries of the images and range between ± 0.004 pixel in the middle and up to ± 0.906 pixel at the borders. In comparison, the discrepancies in y have got the same orientation due to a relatively low oblique RIM photography. The effect decreases to the lower half of the images. It can be assumed that a horizontal exposure axis results in an inversion of the error vectors, equal to the effects in x . The variations in column are in the range of $+0.029$ pixel to 1.088 pixel.

The occurred small systematic errors can be explained by the angle of incidence: Larger angles results in a decrease of the backscattered near-infrared energy. According to Kahlmann's investigations [5], the measured distance becomes longer with an increasing angle of incidence. The systematic displacements in $\pm x$ resp. $+y$ of the centers of the spheres measured in the range images validate this assumption (Fig. 6b).

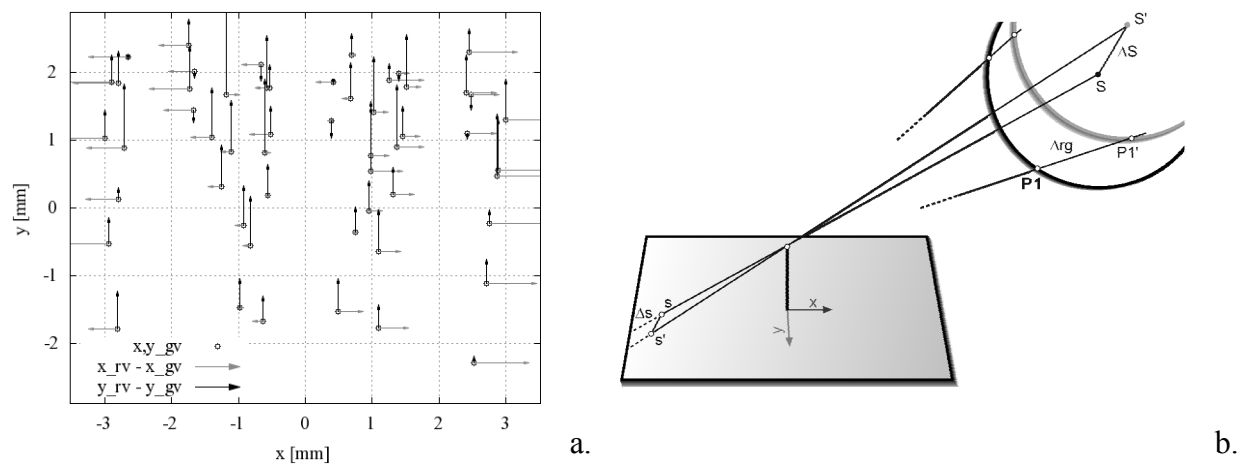


Fig. 6: Influence of the angle of incidence. Left: Variations between intensity and range image point measurements (Exaggeration: 10). Right: Systematic longer measured distances ($+\Delta rg$) of the sphere points cause a systematic displacement of the center of the sphere in image space.

5. Simultaneous Calibration by Integrated Spatial Resection

Combining all 3-D camera observations for a photogrammetric camera calibration allow an adequate utilization of the RIM information content. Beyond the requested camera parameters,

a-priori accuracy specifications of the intensity and range image point measurements as well as the distance measurements become available. Furthermore, the proposed approach can be extended by additional distance calibration terms.

In detail, the following observations are introduced for an integrated camera calibration technique:

1. Targets' pixel coordinates from intensity images (Sec. 4.1).
2. Targets' pixel coordinates from range images (Sec. 4.2).
3. Slant range between perspective center and targets in object space (Sec. 4.2).

5.1. Functional Model

The measured image coordinates $(x,y)_{gv}$ and $(x,y)_{rv}$ determined from gray and range values are used to formulate the collinearity equation for both channels. This results in 4 observation equations per target:

$$\begin{aligned} x^{gv,rv} &= F\left(X_0, Y_0, Z_0, \omega, \varphi, \kappa, pp_x, cc, dx, X, Y, Z\right) \\ y^{gv,rv} &= F\left(X_0, Y_0, Z_0, \omega, \varphi, \kappa, pp_y, cc, dy, X, Y, Z\right) \end{aligned} \quad \begin{array}{l} Z_0, X_0, Y_0: \text{ Perspective center} \\ \omega, \varphi, \kappa: \text{ Rotation angles} \\ pp: \text{ Principal point} \\ cc: \text{ Focal length} \\ dx, dy: \text{ Distortion parameters} \\ X, Y, Z: \text{ Target in object space} \end{array} \quad (2)$$

In addition, one observation equation per target can be introduced for the slant range between the unknown perspective center and the 3-D coordinates of the targets:

$$rg(x,y)^{gv,rv} = \sqrt{\left(X - X_0\right)^2 + \left(Y - Y_0\right)^2 + \left(Z - Z_0\right)^2} + \Delta rg \quad (3)$$

In a first instance, the uncertainties of the distance measurement are modeled straightforwardly by an additive correction term Δrg .

5.2. Stochastic Model

The proposed integrated calibration approach combines heterogeneous observations and requires adjusted weights to tap the full information potential. Westfeld and Hempel [13] already show by robust variance covariance matrix estimation that an aggregation of all observations of one group with one weight is acceptable. Based on this work, the weights for each group of observations are computed by iterative variance component estimation (VCE). See [7] for further information for the computation. As a result, the variances (and therewith the a-priori SD) for the gray and range value image point measurements as well as the distance measurement become available.

5.3. Results

The integrated resection has been parameterized with the parameters of the IOR, which model the camera's geometry,

- focal length cc ; principal point pp ; image distortions $A1, A2, B1, B2, C1, C2$,

and the EOR parameters

- perspective center X_0, Y_0, Z_0 ; a, b, c, d as algebraic parameters for the rotation matrix

as well as an additive distance correction term

- Δrg

For each adjustment, the significance level of the introduced parameters was tested by a 1-D student test ($p=0.95$).

The following Tab. 1 and 2 show the resulting parameters and their SD. Tab. 3 shows the overall accuracy and the a-priori SD of the original as well as the a-posteriori SD of the adjusted observations. For comparison, multiple (integrated) spatial resections were performed using either image points measured in intensity (Tab. 1-3, row 1) resp. range images only (Tab. 1-3, row 2) or heterogeneous groups of observations (Tab. 1-3, row 3; Tab. 3, row 4).

Observations	cc [mm]	pp_x [mm]	pp_y [mm]	$A1$	$A2$	$B1$	$B2$	$C1$	$C2$
$(x,y)_{gv}$	7.860 0.0088	0.203 0.0150	0.685 0.0141	-0.003 1.378·E-4	3.21·E-5 9.653·E-6	6.19·E-4 8.724·E-5	0.002 6.315·E-5	0.004 4.355·E-4	-0.002 4.378·E-4
$(x,y)_{rv}$	7.851 0.0414	0.064 0.0192	0.311 0.054	-0.002 1.512·E-4	×	×	×	×	×
$(x,y)_{gv,rv}$ $(rg)_{rv}$	7.860 0.0088	0.202 0.0149	0.684 0.0140	-0.003 1.376·E-4	3.26·E-5 9.642·E-6	6.15·E-4 8.715·E-5	0.002 6.308·E-5	0.004 4.349·E-4	-0.002 4.371·E-4

Tab. 1: Parameters of the IOR and their SD.

Observations	X_0 [mm]	Y_0 [mm]	Z_0 [mm]	a	b	c	d	Δrg [mm]
$(x,y)_{gv}$	2797.436 1.4979	978.271 0.4468	1184.840 0.8805	0.361 7.924·E-4	0.350 8.321·E-4	0.646 4.282·E-4	0.574 4.482·E-4	×
$(x,y)_{rv}$	2782.595 7.0692	976.195 1.2444	1162.159 4.3512	0.343 0.0022	0.341 0.0023	0.656 0.0013	0.579 0.0012	×
$(x,y)_{gv,rv}$ $(rg)_{rv}$	2797.364 1.4959	978.267 0.4460	1184.698 0.8793	0.3612 7.930·E-4	0.350 8.337·E-4	0.646 4.284·E-4	0.574 4.489·E-4	512.583 4.371·E-4

Tab. 2: Parameters of the EOR and additive range correction term and their SD.

Observations	σ_0 [pixel]	$\hat{\sigma}_0$ [pixel]	$\sigma_{x,y}^{gv}$ [pixel]	$\sigma_{x,y}^{rv}$ [pixel]	σ_{rg}^{rv} [mm]	$\hat{\sigma}_{x,y}^{gv}$ [pixel]	$\hat{\sigma}_{x,y}^{rv}$ [pixel]	$\hat{\sigma}_{rg}^{rv}$ [mm]
$(x,y)_{gv}$	1.000	0.037	1.000	×	×	0.013	×	×
$(x,y)_{rv}$	1.000	0.199	×	1.000	×	×	0.062	×
$(x,y)_{gv,rv}$	1.000	1.000	0.038	0.402	×	0.013	0.013	×
$(x,y)_{gv,rv}$ $(rg)_{rv}$	1.000	1.000	0.038	0.402	22.542	0.013	0.013	3.070

Tab. 3: Overall accuracies, a-priori and a-posteriori SD of the observations.

The overall accuracy for a single channel estimation (Tab. 3, row 1-2) are in a range of $1/30$ pixel for intensity image points resp. $1/5$ pixel for the range one. The IOR and EOR parameters could be determined precisely and significantly by usual intensity measurements (Tab. 1-2, rows 1). The dimension of the values corresponds with previous results (cf. e.g. [3] [15]). As expected, the precision decreases by a factor of 5 using range image information only (Tab. 1-2, rows 2).

The a-priori SD of the observations should be in the range of the accuracies of the input values. 2-D LSM determines the translation parameters with an accuracy of up to $1/40$ pixel (Sec.

4.1). In comparison, the SD of the intensity channel was estimated worse by VCE and becomes $1/26$ pixel (Tab. 3, rows 3-4). A reason for this is that the 2-D LSM SD is only an analytic error estimate. Nevertheless, the dimensions of the SD are quite good; the residuals do not show any systematic effects and are in a range of $1/35$ pixel (Fig. 7a). The a-priori SD of the image coordinates gained from range value observations is stated with $1/2-1/3$ pixel; in contrast to $1/10$ pixel obtained from the image analysis scheme presented in Sec. 4.2. The SD of the sphere fits are a measure for the internal quality only and do not reflect the remaining systematic errors identified in Sec. 4.3 and Fig. 7.

The slant range between perspective center and target has been introduced as a further observation group. Thus it is possible to determine the precision of the distance measurement and integrate additional distance correction terms. As mentioned in Sec. 5.1, the presented work mainly concentrates on a photogrammetric calibration and considers a simple additive correction term only. The a-priori SD of the distance measurements can be specified with 23 mm, which is a comprehensible dimension for such a 3-D measuring device. The a-posteriori SD is still about 3 mm, which indicates the need for a suitable distance calibration.

The a-posteriori overall accuracies of the integrated spatial resections (Tab. 3, rows 3-4) correspond with the set a-priori values, which indicates a well performed VCE.

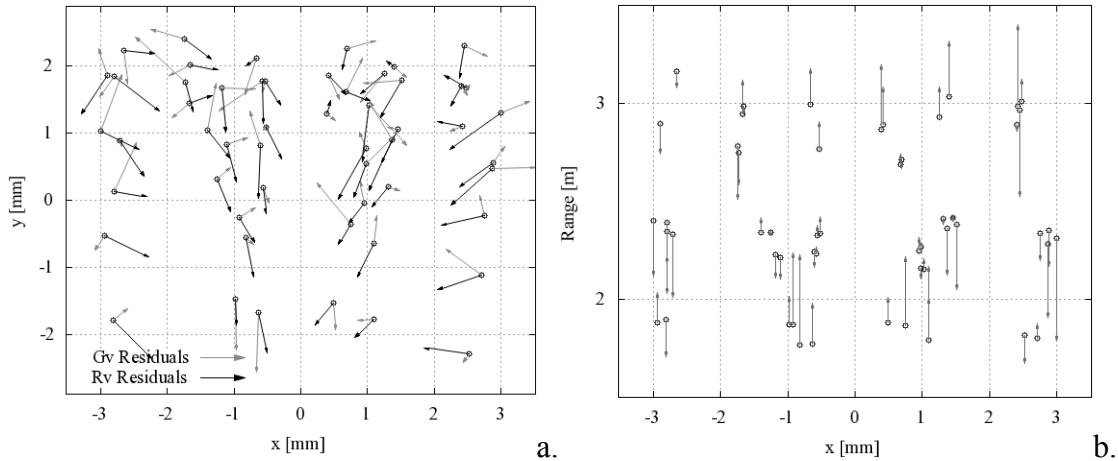


Fig. 7: Residuals of the adjustment. Left: Intensity and range image points. Exaggeration: 25 resp. 250. $\bar{v}_{gv} = \pm 1/35$ pixel resp. $\bar{v}_{rv} = \pm 1/3$ pixel. Right: Distance measurements. Exaggeration: 10. $\bar{v}_{rg} = \pm 18.12$ mm.

6. Conclusion and Outlook

The presented work combines RIM intensity and range data in an integrated photogrammetric calibration approach which results in the queried IOR parameters including their SD. As expected, the range image points as well as the slant ranges as additional observations do not result in a significant increase of parameter's accuracies. However, the adjustment becomes more robust due to an enhanced amount of different observations. Furthermore, a-priori accuracy information of the introduced observation groups become available.

Up to now, the experimental effort is relatively high due to numerous positioning of the moving calibration plate. Assuming an increase of the spatial resolution in the course of further 3-D camera technology developments allow a reduction of the size of the spheres (and therewith a higher number of spheres per plate).

Future work will concentrate on the following aspects:

- Experimental validation of the sphere fit by nominal/actual value comparison.
- Substituting the additive distance correction by a more suitable calibration term. At this it is possible to use the experiences gained from e.g. Kahlmann [5] or Karel [6].
- Combining sphere fits, photogrammetric and distance calibration in one adjustment.
- Performing further experimental setups using 3-D cameras of the most current generation (MESA's *SwissRanger SR-4000* resp. PMDTec's *CamCube*).

References:

- [1] Burkhart, S.: Automatische Messung kreisförmiger Zielmarken, Unveröffentlichte Studienarbeit, TU Dresden, IPF, 2007.
- [2] Fischler, M. A. and Bolles, R. C.: Random sample consensus: a paradigm for model fitting with applications to image analysis and automated cartography, *Commun. ACM* (24:6), 1981, pp. 381-395.
- [3] Hempel, M.: Validierung der Genauigkeit und des Einsatzpotentials einer distanzmessenden Kamera. Unveröffentlichte Diplomarbeit, TU Dresden IPF, 2006.
- [4] Kahlmann, T., Remondino, F. and Ingensand, H.: Calibration for increased accuracy of the range imaging camera *SwissRanger*, *ISPRS*, 2006, pp. 136 ff.
- [5] Kahlmann, T.: Range imaging metrology - investigation, calibration and development, Diss., Eidgenössische Technische Hochschule ETH Zürich, Nr. 17392, 2007.
- [6] Karel, W.: Integrated Range Camera Calibration Using Image Sequences from Hand-Held Operation, *ISPRS08*, 2008, pp. B5: 945 ff.
- [7] Koch, K.-R. Parameterschätzung und Hypothesentests in linearen Modellen, Ferd. Dummlers Verlag, Bonn, 2004.
- [8] Lichti, D.: Self-Calibration of a 3D Range Camera, *ISPRS08*, 2008, pp. B5: 927 ff.
- [9] Lindner, M. and Kolb, A.: Lateral and Depth Calibration of PMD-Distance Sensors, *International Symposium on Visual Computing (ISVC06)*, Springer, 2006, pp. 524-533.
- [10] Luhmann, T.: *Nahbereichsphotogrammetrie: Grundlagen, Methoden und Anwendungen*, Vol. 2., überarb. A. (1. Juli 2003), Wichmann, 2003.
- [11] Robbins, S., Schroeder, B., Murawski, B., Heckman, N. and Leung, J.: Photogrammetric calibration of the *SwissRanger* 3D range imaging sensor, *Society of Photo-Optical Instrumentation Engineers (SPIE) Conference Series*, 2008.
- [12] Schiller, I., Beder, C. and Koch, R.: Calibration of a PMD-Camera Using a Planar Calibration Pattern Together with a Multi-Camera Setup, *ISPRS08*, 2008, pp. B3a: 297 ff.
- [13] Schwarte, R.: Verfahren und Vorrichtung zur Bestimmung der Phasen- und/oder Amplitudeninformation einer elektromagnetischen Welle. Patentschrift DE 19704496, Inhaber Schwarte GBR, 1997.
- [14] Westfeld, P. and Hempel, R.: Range Image Sequence Analysis by 2.5-D Least Squares Tracking with Variance Component Estimation and Robust Variance Covariance Matrix Estimation, *ISPRS08*, 2008, pp. B5: 457 ff.
- [15] Westfeld, P.: Ansätze zur Kalibrierung des Range-Imaging-Sensors SR-3000 unter simultaner Verwendung von Intensitäts- und Entfernungsbildern, in Luhmann, T., ed., *Photogrammetrie - Laserscanning - Optische 3D-Messtechnik (Beiträge Oldenburger 3D-Tage 2007)*, Herbert Wichmann Verlag Heidelberg, 2007, pp. 137 ff.